ELSEVIER

June 1994

Optical Materials 3 (1994) 115–121

OPTICAL Materials

Absolute non-radiative energy conversion efficiency scanning imaging of growth defects in Ti^{3+}: Al_2O_3 crystals using quadrature photopyroelectric detection

S. Buddhudu, J. Vanniasinkam, A. Mandelis, B. Joseph

Photothermal and Optoelectronic Diagnostics Laboratory, Department of Mechanical Engineering, University of Toronto, Toronto, M5S 1A4 Canada

K. Fjeldsted

Crystar Research Inc., Victoria, British Columbia, V8Z 3B6 Canada

Received 20 September 1993

Abstract

Quadrature lock-in photopyroelectric spectroscopic (PPES) (Q-scanning) imaging of Czochralski-grown Ti:Sapphire crystals was investigated at 490 nm using a novel non-contact experimental configuration. Simultaneous optical absorption coefficient, $\beta(r)$, scans were obtained from the PPES signal in the purely optical transmission (in-phase) lock-in mode. The quadrature scans were further converted to absolute non-radiative energy conversion efficiency, $\eta_{NR}(r)$, images using the in-phase-generated $\beta(r)$ data and PPES theory. The quadrature and $\eta_{NR}(r)$ images exhibited superior resolution and sensitivity to growth defect (bubble) clusters than the $\beta(r)$ images. Therefore, Q- and η_{NR}- scanning imaging can be used as an effective monitoring criterion of crystal growth and processing quality control in Ti:Sapphire and, generally, in optical materials.

1. Introduction

Photopyroelectric spectroscopy (PPES) has been used for the measurement of the optical-to-thermal (non-radiative) energy conversion efficiency, η_{NR}, with considerable success [1–4]. The materials for which PPES η_{NR} studies have been reported have mostly been solids with relatively high non-radiative efficiencies, e.g. bulk and amorphous thin-film semiconductors [2–4], and optical quality Nd_2O_3 powders dispersed in a PMMA matrix [1], exhibiting $\eta_{NR} \sim 0.83$–0.92. Recent reviews can be found in Refs. [5] and [6]. In the case of optical and fluorescent materials Chirtoc et al. [7] measured $\eta_{NR}(\lambda)$ of dye inks containing Rhodamine B and Coumarin 6. The reported optical absorptions and optical-to-thermal energy conversion efficiencies were sizable, so that acceptable signal-to-noise ratios (SNR) could be obtained with the sample contacting the pyroelectric sensor element (polyvinylidene fluoride, PVDF). On the other hand, in the case of transparent, high-quality laser materials, $\eta_{NR}(\lambda)$ is typically expected to be a maximum of a few percent [8,9]. For measurements with this type of optical materials conventional contacting PPES was found to be hard to use, because the small thermal contribution to the signal must be extracted very accurately from the mixed optical and thermal signal modes. Very recently we developed a novel noncontact experimental configuration [10] to obtain high-resolution absolute spectra

SSDI 0925-3467(94)00010-N

of $\eta_{NR}(\lambda)$ of $Ti^{3+}:Al_2O_3$ laser crystals with widely different figures of merit. The advantages of the non-contact geometry, Fig. 1, are (i) the absence of irreproducible thermal resistances (always present at the sample–PVDF interface in the contact mode); and (ii) the presence and the high degree of controllability of the airgap layer of variable thickness L. This allows for optimally efficient suppression of the direct optical heating mode of the sensor element itself (in-phase lock-in signal) and for easy, reproducible monitoring of the purely thermal-wave signal (lock-in quadrature) which is directly proportional to $\eta_{NR}(\lambda)$. It has been shown [10] that the total suppression of the much stronger in-phase signal (more than two orders of magnitude higher than the quadrature) allows the measurement of minute optical-to-thermal energy conversion efficiencies $\eta_{NR} \sim 1.9$–13.8% in Ti:Sapphire. To put the sensitivity of this new non-contact PPE spectrometer in perspective, Coufal measured phase shifts in the 0.1–0.9° range with his fixed-thickness, contacting, thermal-wave "phase shifter" with ca. 0.1° phase resolution [1]. He was thus able to measure η_{NR} in the 0.55–0.9 range. By comparison, our method of quadrature detection using an absorption-free highly controllable variable-thickness thermal-wave phase shifter (i.e. the backing airgap layer) allowed the measurement of minute signals corresponding to phase shifts in the 0.02–0.2° range with 0.015° phase resolution. Based on this order-of-magnitude improvement of quadrature PPES signals, in this work we report the first scanning imaging application using the new PPE spectrometer and Ti:Sapphire wafers with growth-induced bulk defects. Our results clearly show the superior resolution of the defect regions mapped as non-radiative centers during the quadrature scan, as compared to conventional optical transmission imaging.

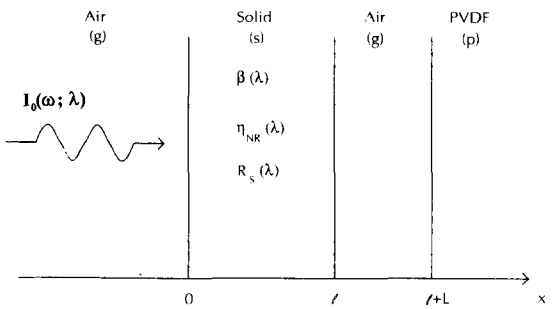

Fig. 1. Schematic geometry of non-contact PPES of a transparent sample of thickness l, optical absorption coefficient $\beta(\lambda)$, and non-radiative energy conversion efficiency $\eta_{NR}(\lambda)$. Air layer thickness L; semi-infinite PVDF detector. Optical modulation angular frequency: ω; incident optical intensity I_0.

2. Experimental and results

2.1. Materials preparation

Crystals of $Ti^{3+}:Al_2O_3$ were grown by the Czochralski pulling technique from a molten mixture of Al_2O_3–Ti_2O_3. The growth conditions were: ambient atmosphere of nitrogen with trace of oxygen; pulling rate is 6×10^{-2} in/h; rotation rate is 5 rpm. The seed was sapphire 90° (off C-axis) A orientation. Crystals were grown 2.5″ in diameter. Some crystals were further annealed at 1850°C for 100 h in Ar atmosphere. Bubble clusters were visible in concentric patterns centered at the crystal boule rotation axis. These microbubble clusters were most likely due to thermal gradients within the Ir crucible.

The PPE investigation involved wafers of 0.15 cm thickness cut from both unannealed and annealed boules. Grinding and polishing resulted in smooth surface finishes and uniform thicknesses.

2.2. Scanning imaging and spectroscopy

Non-contact photopyroelectric scanning imaging and spectroscopy were performed on unannealed and annealed Ti:Sapphire wafers using instrumentation conforming to the geometry of Fig. 1. The schematic of this apparatus is shown in Fig. 2. The 1000 W Xe lamp was used for scanning imaging at 490 nm instead of a laser, so as to produce large enough filament images (lateral spot dimensions $\gg$ sample-detector distance L) for a one-dimensional theoretical treatment of the PPES signal to remain valid [10]. Further details of the experimental set-up can be found in Ref. [10]. Optical absorption coefficient scanned images and spectra were obtained photopyroelectrically in the purely optical transmission mode ($L\to\infty$) [10]. The condition $L\to\infty$ could be satisfied in the thermally thick gas layer for $L\geq5$ mm at chopping frequency $f=9$ Hz. It was necessary to record scans and spectra within the same experimental

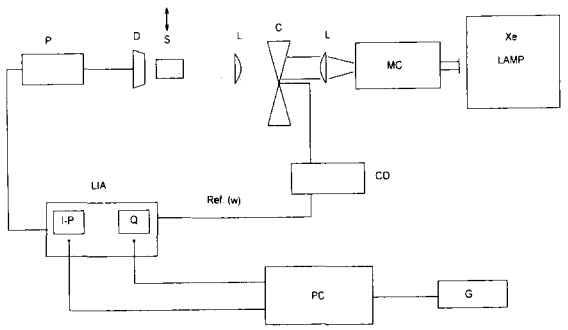

Fig. 2. Schematic of non-contact PPES scanning imager and spectrometer. MC: monochromator, L: lens, C: chopper, S: sample and (x, y) scanning stage, D: blackened PVDF detector, P: pre-amplifier with adjustable bandpass filters, LIA: lock-in amplifier (EG & G Model 5210 in I-P and Q mode), CD: chopper driver, PC: computer for data acquisition, processing and theoretical analysis, G: graphics and plotter.

period for each sample and after complete thermalization of the instrumentation (ca. one hour after turn-on), in order to obtain reproducible results. Optical transmission scans were normalized by the Xe lamp throughput at 490 nm. The reflectance spectra, $R_s(\lambda)$, of the Ti:Sapphire samples were recorded and absolute values of $\beta(\lambda)$ or $\beta(x, y)$ were obtained using the following formula [10]:

$$\beta = -\frac{1}{l}\ln\left\{\frac{(1-R_s)^2}{2R_s^2\rho_\infty}\left[\sqrt{1+\left(\frac{2\rho_\infty R_s}{1-R_s^2}\right)^2}-1\right]\right\}, \tag{1a}$$

where

$$\rho_\infty(\lambda) \equiv V_\infty(\omega;\lambda)/V_R(\omega;\lambda)\,. \tag{1b}$$

In Eq. (1), V_∞ and V_R represent the PPE voltage with the sample in place at $L=\infty$ (purely optical mode), and without the sample (reference mode), respectively. Fig. 3 shows typical optical absorption coefficient scans for an unannealed (Fig. 3a) and an annealed (Fig. 3b) Crystar wafer. The center of the wafer disks was at $(x, y) = (0.2\text{ cm}, 0\text{ cm})$. The essentially monotonic increase of $\beta(x, y)$ along the $y>0$ quadrant is at least partly due to increased microbubble densities in the region $y>0.8$ cm for both crystal wafers. For this reason the measured values of $\beta(x, y)$ are not considered reliable, given that significant light scattering occurred in the bubble/defect-rich regions, which tended to increase the effective β value artificially. Therefore, the axis normal to the (x, y)-

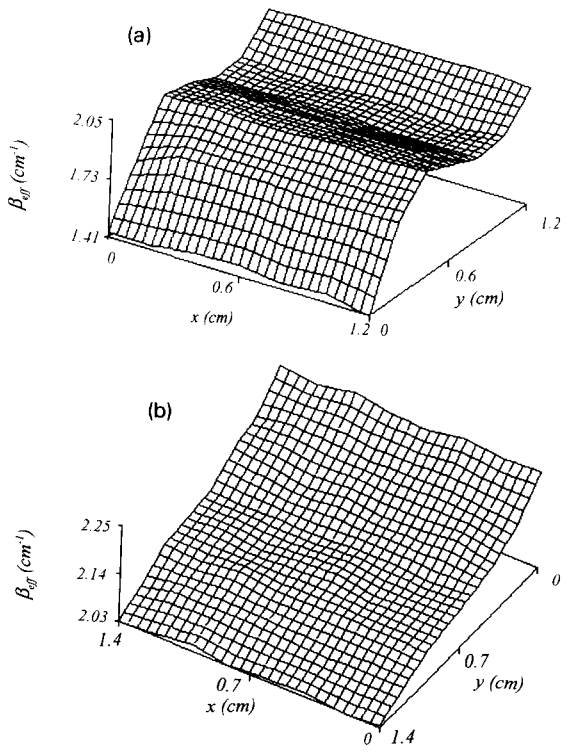

Fig. 3. Scanning imaging of effective optical absorption coefficients $\beta_{eff}(x, y)$, at 490 nm with 8 nm resolution. Center of Ti:Sapphire wafers is located at $(x,y) = (0.2\text{ cm}, 0\text{ cm})$. Wafer radius: 3.175 cm; wafer thickness: 0.15 cm. (a) unannealed, and (b) annealed sample.

plane in Fig. 3 has been labelled β_{eff}, since the scattering coefficient could not be measured. It was further discovered that the reproducibility of the β_{eff} scans was poor and so was the defect-rich region resolution. For instance, no sign of a small defect cluster at the centers of the wafers can be seen in these scans. Fig. 4 shows $\beta_{eff}(\lambda)$ spectra obtained in four locations on the unannealed wafer, which exhibited more pronounced defect clusters than the annealed wafer Spectra (1) and (2) correspond to visually defect-free regions, whereas spectra (3) and (4) were obtained in defect-rich areas. These spectra are characterized by relatively poor reproducibility, which most likely stems from the fact that repeated scans may not result in perfect repositioning of the optical beam on the same defect cluster neighborhood. Furthermore, the presence of readily visible and invisible bulk defects has resulted in gross distortions of spectral features, when compared to spectra obtained using de-

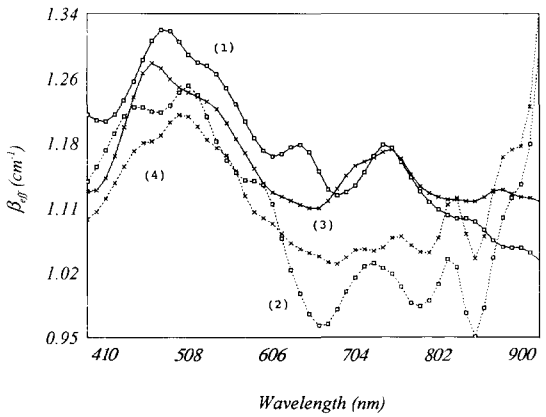

Fig. 4. PPE spectra of $\beta_{eff}(\lambda)$ from the unannealed wafer of Fig. 3a, corresponding to (1): defect-free ring between center and $x=y=1.2$ cm; (2): defect-free region $(x, y) \approx z$ (2 cm, 2 cm); (3): defect-rich center $(x, y) \approx (0.2$ cm, 0 cm); and (4): defect-rich ring at $(x, y) = (1.2$ cm, 1.2 cm). Chopping frequency: 9 Hz.

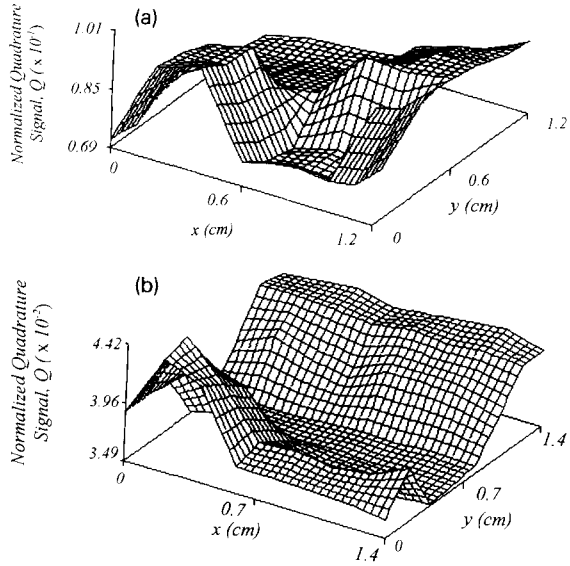

Fig. 5. Scanning imaging of normalized PPE quadrature, $Q(x, y)$, at 490 mn corresponding to Fig. 3 (a) unannealed, and (b) annealed sample.

fect-free Ti:Sapphire crystals [10]. In Fig. 4 it should be noted that normal lineshape is exhibited only by curve (1), the visually defect-free region surrounding a small cluster at the center. In fact, the only normal features of this curve are the position of the broad peak centered around 470 nm and corresponding to the $^2T_{2g} \rightarrow {}^2E_g$ transition broadened by phonons, and the low energy side shoulder due to the Jahn–Teller splitting of the ^2E_g (upper) state [11]. The rest of the curves exhibit these fundamental $Ti^{3+}:Al_2O_3$ features distorted, including the nominally defect-free region (2). This is consistent with the scan of Fig. 3a and with the thermal scan of Fig. 5, below. It is indicative of microdefect densities which are not readily visible.

Thermal energy generation images were recorded at 490 nm simultaneously with "infinite distance" (purely optical) scans, by decreasing the distance L to some pre-determined value < 1 mm where a measurable stable lock-in quadrature signal was present. Experimentally, the quadrature of the signals corresponding to "infinite" and "finite" L-distances were subtracted at each (x_j, y_j) location in order to cancel out photoyroelectric phase shifts induced by different d.c. optical heating levels of the polymer PVDF as the transmitted optical flux varied throughout the scan, as indicated in Fig. 3.

Fig. 5 shows quadrature (Q) scans of the wafer regions whose β_{eff} are shown in Fig. 3. The Q-signal levels are ca. two orders of magnitude lower than the respective IP-signals which led to Fig. 3, as expected [10]. It is immediately apparent that the Q-scans are much more structured than the β_{eff} scans. Particularly, defect-rich cluster regions at the wafer center, the defect-free intermediate zone and the outer defect ring of the unannealed sample can be clearly seen in Fig. 5a. This detail is to be contrasted with the nondescript β_{eff} image of Fig. 3a. The structure shown in Fig. 5a directly corresponds to visual information which can be "seen" when the wafer is held under Ar^+-ion laser illumination. Therefore, it is hypothesized that the optical image of Fig. 3a is dominated by scattered light effects, which are to a large degree absent from the purely thermal-wave image of Fig. 5a. Much more subtle features are seen in Fig. 5b, which corresponds to the β_{eff} scan of Fig. 3b. Here, annealing has caused the shrinkage of large defect clusters observed in Fig. 5a, with a small cluster at the wafer center still visible under Ar^+-ion laser illumination. The increasing β_{eff} for $y > 0$ values in Fig. 3b has some corresponding features in Fig. 5b for $y > 0.7$ cm. It is interesting to note that the low Q-signal level flat regions of Figs. 5a, b cannot be seen in Figs. 3a, b. More significantly the difference in absolute Q-signal levels between Figs. 5a and 5b is a

strong indicator of the restoration of bulk quality of the Ti:Sapphire crystal following the process of annealing. This important type of information is totally absent from the β_{eff} images. Another strong illustration of the foregoing advantage of the Q-signal can be observed in the spectral behavior of the quadrature, Fig. 6. The numbered spectra, normalized by the PVDF spectrum, correspond one-to-one to the $\beta_{\text{eff}}(\lambda)$ spectra of Fig. 4. In the case of the quadrature spectra, however, distinct separation exists between defect-rich (high signal level) and defect-free (low signal level) locations. Furthermore, the reproducibility of the $Q(\lambda)$ spectra is within 10% of the values shown. Most importantly the labelled order of the spectra (1)-(4) is always strictly reproducible, whereas this is not the case with the $\beta_{\text{eff}}(\lambda)$ spectra of Fig. 4. Similar effects were observed with the annealed crystal, but the absolute values and the spectral level differences between defective and defect-free locations were smaller than those shown in Fig. 6, as expected from the higher quality (impacting absolute signal values) and the higher uniformity (impacting relative signal differences) of that wafer.

3. Data analysis and discussion

Nonradiative energy conversion efficiency images, $\eta_{\text{NR}}(x, y)$ and spectra, $\eta_{\text{NR}}(\lambda)$ were derived from the Q-signals, i.e. from the purely thermal energy generation data shown in Figs. 5 and 6. For this purpose the previously derived PPE quadrature equation was used (Eq. (20) in Ref. [10]):

$$Q(x, y; \lambda) \equiv \text{Im}(V_{\text{L}}/V_{\text{R}})$$
$$\approx -\eta_{\text{NR}}(x, y; \lambda) b_{\text{gs}} F(R_{\text{s}}, \beta_{\text{eff}} l, L, \omega, \alpha_{\text{s}}) , \qquad (2)$$

where V_{L} represents the PPE voltage at a sample-detector distance L; b_{gs} is the thermal coupling coefficient of the gas (air)–solid (crystal) interface; F is a complicated function of the crystal surface reflectance, R_{s}, the absorptance ($\beta_{\text{eff}} l$) product, the gas-layer thickness, L, the modulation angular frequency, ω, and the thermal diffusivity, α_{s}, of the crystal. Eq. (2) shows that the PPE quadrature signal is directly proportional to η_{NR}. As indicated by Eq. (2), the function F was calculated with an IBM PC for every (x_j, y_j) location on the scanned wafers, using data from Figs. 3 and 5. This resulted in absolute nonradiative energy conversion efficiency images as shown in Fig. 7. Qualitatively, only slight variations from the Q-scans can be observed. The observed higher non-radiative energy conversion efficiency for the unannealed sample can be understood in terms of the latter being a poorer photon generator, thus yielding a lower level of luminescence than the an-

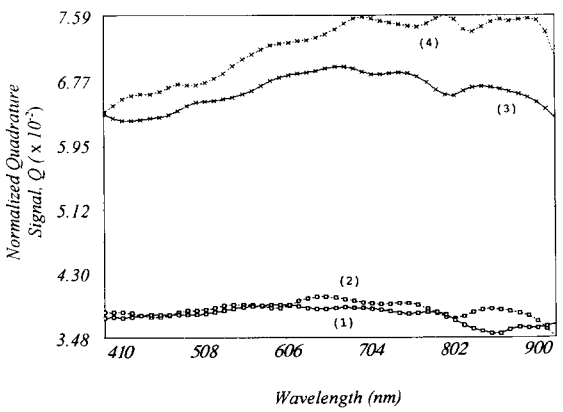

Fig. 6. PPE quadrature spectra corresponding to the unannealed wafer locations of Fig. 4. There is a one-to-one correspondence between curves (1)-(4) in both figures.

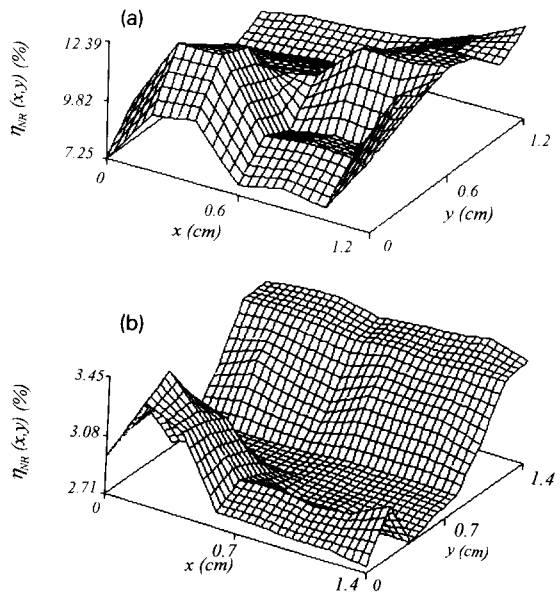

Fig. 7. Scanning imaging of absolute non-radiative energy conversion efficiency corresponding to a combination of the scans in Figs. 3 and 5, according to Eq. (2), (a) unannealed, and (b) annealed sample.

nealed sample, which is therefore overall better suited for laser rod fabrication. The reliability of η_{NR}-scans is, however, poorer than that of the original Q-scans, because the somewhat ill-reproduced $\beta(x, y)$ data must be used as an input to construct the $\eta_{NR}(x, y)$ images. Nevertheless, both sets of Figs. 5 and 7 clearly show the wafer regions which are most suitable for laser materials fabrication, namely the low-lying signal "valleys". This important information cannot be retrieved from the optical images of Fig. 3 alone, and emphasizes the superior nature of $\eta_{NR}(x, y)$ imaging. For completeness, Fig. 8 shows complete $\eta_{NR}(\lambda)$ spectra corresponding to the spectra of Fig. 6 (Fig. 8a), for the unannealed wafer, as well as spectra from two locations in the annealed wafer (Fig. 8b). The

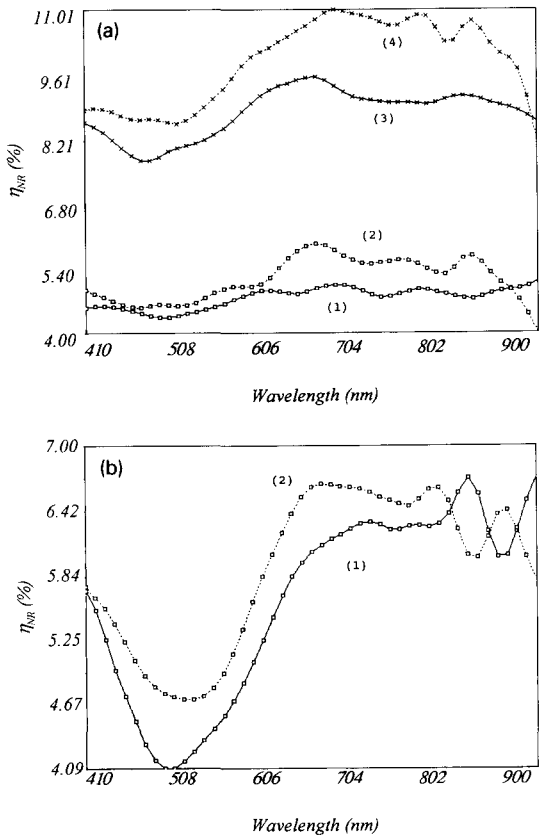

Fig. 8. (a) Non-radiative energy conversion efficiency spectra from the unannealed wafer obtained through the combination of spectra shown in Figs. 4 and 6. The labels (1)-(4) correspond to the respective curves in those figures. (b) Similar spectra obtained from the annealed wafer: curve (1) is from the "valley" region of Fig. 7b; curve (2) is from the center of the wafer at $(x, y) = (0.2\text{ cm}, 0\text{ cm})$ in Fig. 7b.

difference in absolute values of η_{NR} between the groups of spectra taken at defect-free (curves 1, 2) and defect-rich regions (curves 3,4) of the unannealed sample in Fig. 8a is much more pronounced than the respective curves of the annealed sample, Fig. 8b. This fact constitutes further evidence of the partial homogenization of the Ti:Sapphire crystals induced by the annealing process. The spectral lineshapes of $\eta_{NR}(\lambda)$ from the unannealed wafer are fairly distorted compared to our earlier spectra with defect-free high-quality Ti:Sapphire crystals [10]. The lineshape curve (1), Fig. 8b from the annealed wafer is, however, similar to the earlier ones, yet curve (2) exhibits some degree of spectral distortion, especially at the η_{NR} minimum around $\lambda = 510$ nm.

4. Conclusions

In this work we used a modified, non-contacting, high-sensitivity quadrature photopyroelectric detection scheme to obtain pure optical-to-thermal energy conversion efficiency images of Ti:Sapphire wafers prepared from unannealed and annealed crystals. Both the quadrature and the derivative nonradiative energy conversion efficiency images demonstrated superior defect diagnostic ability to conventional optical absorption coefficient scans. Therefore, they may be useful as a quality control imaging technique for crystal growth, as well as for investigations into the nature of bulk Ti:Sapphire defects and their role in the optical quality of this material when it is used as a tunable solid-state laser.

Acknowledgements

We gratefully acknowledge a Strategic Grant from the Natural Sciences and Engineering Research Council of Canada (NSERC), which made this work possible.

References

[1] H. Coufal, Appl. Phys. Lett. 45 (1984) 516.
[2] A. Mandelis, R.E. Wagner, K. Ghandi, R. Baltman and P. Dao, Phys. Rev. B 39 (1989) 5254.

[3] J. Fan and J. Kakalios, Phil. Mag. Lett. 64 (1991) 235.
[4] C. Christofides, A. Mandelis and K. Ghandi, Rev. Sci. Instrum. 61 (1990) 2360.
[5] A. Mandelis, Condensed Matter News 2, 3 (May/June 1993).
[6] C. Christofides, Crit. Rev. Solid State Mat. Sci. 18 (1993) 113.
[7] M. Chirtoc, R.M. Candea and J. Pelzl, Appl. Spectrosc. 47 (1993) 1071.
[8] R.S. Quimby and W.M. Yen, J. Appl. Phys. 51 (1980) 1780.
[9] M.L. Shand, J. Appl. Phys. 54 (1983) 2602.
[10] A. Mandelis, J. Vanniasinkam, S. Buddhudu, A. Othonos and M. Kokta, Phys. Rev. B1 48 (1993) 6808.
[11] P.F. Moulton, J. Opt. Soc. Am. B 3 (1986) 125.